PROPERTIES OF A GALAXY IN DEEP MULTI-WAVELENGTH SURVEYS

A thesis submitted towards partial fulfilment of

BS-MS Dual Degree Programme

by

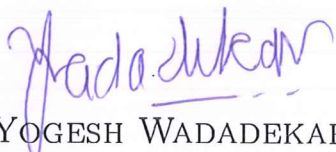TAMHANE PRATHAMESH DHANANJAY

under the guidance of

DR. YOGESH WADADEKAR

NATIONAL CENTRE FOR RADIO ASTROPHYSICS, TATA

INSTITUTE OF FUNDAMENTAL RESEARCH, PUNE

INDIAN INSTITUTE OF SCIENCE EDUCATION AND RESEARCH

PUNE

Certificate

This is to certify that this thesis entitled **Properties of a galaxy in deep multiwavelength surveys** submitted towards the partial fulfilment of the BS-MS dual degree programme at the Indian Institute of Science Education and Research Pune represents original research carried out by **Tamhane Prathamesh Dhananjay at National Centre for Radio Astrophysics, TATA Institute of Fundamental Research, Pune**, under the supervision of **Dr. Yogesh Wadadekar, Reader-F, NCRA-TIFR, Pune** during the academic year 2014-2015.

DR. YOGESH WADADEKAR
(Thesis Supervisor)

Place: Pune
Date: 25 March, 2015

Declaration

I hereby declare that the matter embodied in the report entitled **Properties of a galaxy in deep multiwavelength surveys** are the results of the investigations carried out by me at **National Center for Radio Astrophysics, TATA Institute of Fundamental Research, Pune**, under the supervision of **Dr. Yogesh Wadadekar** and the same has not been submitted elsewhere for any other degree.

TAMHANE PRATHAMESH
DHANANJAY
(Reg. No. 20101065)

Place: Pune
Date: 25 March, 2015

Acknowledgements

Abstract

The evolution of distant galaxies with redshift 0 < z < 2 can be observationally determined by separately tracing the evolution of stars, gas and dust in these galaxies. To do this effectively, one needs to use far-infrared data to trace the dust; ultraviolet, optical and radio data to trace star formation and H-alpha and HI radio observations to trace the ionised and neutral gas, respectively. In addition, we can combine optical spectroscopy with X-ray and radio imaging to understand the properties of the supermassive black holes at the centres of galaxies that manifest as Active Galactic Nuclei. In this project, we used archival observations at many wavelengths from a number of space and ground based facilities such as XMM/Newton, Spitzer, Subaru, VLA and GMRT.

We investigated the nature of extended, diffuse, radio and X-ray emission associated with the lobes of a giant radio galaxy J021659-044920 at redshift $z = 1.325$. X-ray emission is nearly co-spatial with the radio lobes and $0.3 - 10$ keV spectrum can be best fitted with a power law of photon index 1.86, consistent with its plausible origin as Inverse Compton scattering of the Cosmic Microwave Background (ICCMB) photons. We estimate the magnetic field in radio lobes using both X-ray and radio observations. Using both X-ray and radio observations we estimate the magnetic field in the lobes to be 3.3 μG. The magnetic field estimate based on energy equipartition is ~ 3.5 μG. Assuming ICCMB, we estimated minimum energy in the particles in the lobes to be 4.2×10^{59} erg. Notably, radio and X-ray emission from the central AGN remains undetected in present observations inferring that the AGN activity has recently stopped. Our work present a case study of a rare example of a giant radio galaxy caught in dying phase in the distant universe.

Contents

Chapter 1

Introduction

Understanding of the stars, galaxies, the universe comes from studying the light emitted by or reflected from these objects. Technological advances in the last few decades led to the development of electronic detectors, enabling us to detect and study light from entire electromagnetic spectrum. We can study the universe at multiple wavelengths. Combination of observing techniques at various regimes of the electromagnetic spectrum can yield deeper insights into the physics of various sources such as stars and galaxies, compared to observing alone in the radio, optical/UV or X-rays.

Multiwavelength observations are important in studying the evolution of distant galaxies. It can be observationally determined by studying the stars, gas and dust in the galaxies. Therefore we need to use infrared data to trace the dust, optical, ultraviolet and radio (UV) data to trace the star formation and X-ray and radio data to study the supermassive black holes at the centres of galaxies that manifest as Active Galactic Nuclei (AGN), and radio galaxies.

Our initial goal of the project was to study spectral energy distributions and statistical properties of different types of galaxies using multiwavelength data. While studying the 'XMM-LSS' field in 0.325 GHz GMRT radio image, I discovered a giant radio galaxy. After this discovery, we decided to study this giant radio galaxy J021659-044920 in detail using multiwavelength observations. We used archival data at various frequencies from X-ray to radio. We detected diffuse X-ray emission nearly co-spatial with the lobes of the galaxy. We propose Inverse-Compton Cosmic Microwave Background (ICCMB) as the reason for observed

diffuse X-ray emission from the lobes of the galaxy.

Several radio galaxies 1.1 show extended X-ray emission. A variety of physical processes may be responsible for X-ray emission over large scales from these objects. These processes include - thermal emission from shocks, as well as synchrotron radiation 2.1 and Inverse-Compton (IC) scattering of seed photons 2.2. The ubiquitous cosmic microwave background (CMB) forms a source of seed photons. Inverse-Compton scattered CMB photons have been detected in the form of diffuse, extended X-rays in several radio galaxies at cosmological distances. For galaxies with redshift $z > 1$, ICCMB emission has been detected from 4C41.17 ($z = 3.8$; Scharf et al., 2003), 4C 23.56 ($z = 2.48$; Johnson et al., 2007), HDF-130 ($z = 1.99$; Fabian et al., 2009), 6C 0905+39 ($z = 1.833$; Blundell et al., 2006; Erlund et al., 2008) and 3C 294 ($z = 1.786$; Fabian et al., 2003).

Whenever IC is the source of the X-ray emission, the radiative lifetimes of (highly energetic) radio synchrotron-emitting electrons are typically shorter than the (less energetic) electrons which give IC emission in the X-ray band. As a consequence, IC emission always traces an older population of particles which may be more diffuse and spatially non-coincident with the radio emission. The flux of the emission depends on the energy density of the target photons, which in the case of the CMB rises as $(1 + z)^4$, thus cancelling out the decrease in surface brightness due to cosmological dimming (Schwartz, 2002). This fortunate circumstance makes it relatively easy to probe the magnetic field and electron energy distribution in active galactic nuclei (AGN) lobes at high redshift.

The lifetime of the electrons in the sources scales as $1/\gamma_e$ due to radiative losses. Lorentz factors of $\gamma_e \sim 1000$ are required to upscatter the CMB photons and $\gamma_e \sim 10^4$ (exact values depend on strength of the magnetic field) to generate GHz synchrotron radiation in the radio band. As a result, when the AGN switches off and there is no further injection of relativistic electrons, the IC X-ray emission can last 10 or more times longer than the high-frequency radio emission, as observed with typical sensitivities of current instruments. This can give rise to an inverse Compton ghost (e.g., Fabian et al., 2009) where the X-ray emission from the lobes is detected but the radio emission is absent. We note that more sensitive radio continuum observations may be able to detect the emission from

the radio lobes. Also, since the spectral index of radio lobes are often steep, it becomes easier to detect them at low radio frequencies. When used together with radio observations, ICCMB X-ray fluxes can be used to constrain the local magnetic field experienced by the radio-emitting plasma in the lobes of giant FR II (Fanaroff and Riley, 1974) radio sources (see e.g. Erlund et al. (2006)).

In this thesis, we study a giant FR-II radio galaxy J021659-044920 with ICCMB emission at $z \sim 1.3$. Our source is located in the XMM-LSS field. This well studied deep field has extensive archival data in many wavebands all the way from X-ray through radio. For a reasonably current summary of extant data in this field, we refer the reader to Mauduit et al. (2012). In this chapter, basic concepts and observation techniques in radio astronomy and X-ray astronomy are explained. In Chapter 2, we discuss the relevant radiative processes. In Chapter 3, we discuss the observations and analysis procedure, results are presented in Chapter 4 and they are discussed in Chapter 5. Chapter 6 concludes the thesis. Throughout the thesis, spectral index α is defined such that $S_\nu \propto \nu^{-\alpha}$, where, S_ν is the flux density and ν is the frequency. We used the WMAP9 cosmology with $H_0 = 69.32$ km s^{-1}Mpc^{-1}, $\Omega_0 = 0.29$, and $\Omega_\Lambda = 0.71$.

1.1   Radio Galaxies

Some galaxies are very luminous in the radio band. These galaxies are called radio galaxies. Based on their luminosity, radio galaxies are classified as radio loud or radio quiet. Radio galaxies are radio loud if their luminosity is $\sim 10^{41}$ –10^{46} erg s^{-1} in a band extending from 100 MHz to 10 GHz. This corresponds to 5 GHz luminosity $\gtrsim 10^{25}$ W Hz^{-1}. Radio emission in these galaxies is due to synchrotron radiation process.

Radio galaxies have been observed to be found in a variety of different morphological structures and sizes. Their morphologies range from flat spectrum, unresolved compact sources on one end and complex structures on the other end, with hundreds of kiloparsec in extent, with lobes, hotspots, a compact nucleus and jet-like features. The primary features of radio galaxies are core, lobes, hotspot and jet formed by the supply of radio plasma from Active Galactic Nuclei (AGN). Not

all of these features are seen in all sources. Brief introduction of the components of radio galaxies and their classification adapted from Kembhavi and Narlikar (1999) is given below.

- **Cores:** These are compact sources coinciding with the associated optical counterpart of the radio galaxy. The cores usually have flat power law[1] spectrum or complex spectrum. Because of flat spectrum, their flux stays relatively high at higher frequencies, therefore, they are best detected at GHz frequencies. Cores are found in almost ~ 80 per cent of all radio galaxies.

- **Lobes:** These are extended regions of the radio galaxy. Radio galaxies often have two-sided lobes nearly symmetrically placed on opposite sides of the galaxy. Sizes of the lobes can vary from a few kiloparsecs up to 300 kiloparsecs. Thus, the extent of a radio galaxy including the ends of the lobes can be from hundreds of kiloparsecs (kpc) to megaparsec (Mpc) in some extreme cases. Lobes have power law spectrum with $\alpha > 0.5$. Some galaxies also have C-shaped lobes. They are mostly FRI (see section 1.1.1 for terminology) sources in galaxy clusters, with the ram pressure of the surrounding medium sweeping the lobes backwards as the galaxy moves in the environment. Some lobes have Z- or S-shaped structures. This is believed to be because of the precession of the axis of jets that transport the energy from the core to the extended components. Lobes of radio galaxies typically have power law spectral index of ~ 0.7.

- **Jets:** These are features connecting compact cores to the extended regions. Jets are often narrow and can be smooth or knotty. The size of the jets varies from parsec to kiloparsec scales. When jets are seen on both sides of the central source, they are said to be two-sided. In some more luminous galaxies, jets are one-sided, whereas, in less luminous radio galaxies they are two-sided. The kiloparsec scale jets have power law spectral index of ~ 0.6.

- **Hotspots:** They are very bright components located towards the outer extremities of the lobes of highly luminous sources. They have a linear

---

[1]By convention a power law radio spectrum is said to be flat if $\alpha \leq 0.5$ and steep otherwise.

size of ~ 1 kpc and a power law spectral index in the range of ~ 0.5–1 but usually flatter than the lobes. This is consistent with the interpretation of hotspots as the place where the highly energetic jet hits the ambient medium producing shock. Some energetic particles diffuse into the lobes from the hotspots, providing a continuous supply of energy, as long as the jets are active.

1.1.1 Fanaroff Riley Classification

Fanaroff and Riley (1974) observed that most of the radio sources can be classified in two types based on the surface brightness of relative position of different regions in the morphology of the radio galaxies. They divided the radio galaxies into two categories based on the ratio R_{FR}, the ratio of the distance between highest brightness regions on opposite sides of host galaxy, to the total extent of the radio galaxy. Sources for which $R_{FR} < 0.5$ were called as type I (FRI) and sources with $R_{FR} > 0.5$ were called type II (FRII) sources. It was also found that almost all sources with luminosity $L(178MHz) \lesssim 2 \times 10^{25}\ h_{100}^{-2}$ W Hz^{-1} Str^{-1}, where h_{100} is Hubble constant in units of 100 km/s/Mpc, were of class I while almost all sources with luminosity greater than this value were of class II. There is no sharp dividing line in the luminosity of FRI and FRII sources. There is partial overlap between the two. Properties of FRI and FRII galaxies are discussed below:

- **FRI sources:** These sources have high brightness regions close to but the central region as compared to low-brightness region. The spectrum of the lobes becomes steep towards the outer extremities of the lobes indicating old plasma which has radiated away most of its energy. Jets are found in 80 percent of FRI radio galaxies. FRI sources are often located in rich clusters containing hot X-ray emitting gas. C-shaped galaxies are thought to have originated from FRI like sources, as FRI sources are most likely to produce C-shaped galaxies, when the move in the medium and the lobes sweep back due to ram pressure of the medium.

- **FRII sources:** These sources have their brightest regions towards extremities of the lobes away from the central host as compared to low-brightness

region. They often comprise of bright hotspots in their lobes. Cores and jets in these sources are brighter than those in FRI sources as expected from overall high luminosity of these sources. Jets are found in less than 10 per cent FRII radio galaxies. However, jets in FRII sources are generally smooth and end in hotspots in the lobes, that are well separated.

1.1.2 Giant Radio Galaxies

Giant radio galaxies (GRGs) are radio galaxies whose projected linear size is $\geq$0.7 Mpc (H_0=71 km s^{-1} Mpc^{-1}, $\Omega_m = 0.27$, $\Omega_\Lambda = 0.73$). They are very useful in studying various problems in astrophysics and are largest single objects in the universe. The largest GRG known, hosted by a galaxy called as J1420-0545, has linear projected size of 4.7 Mpc. Till today $\sim$120 GRGs are known. Most giant radio sources are FRII but some lie at the boundary of FRI and FRII. The GRG discovered by us is radio loud FRII GRG having 5 GHz spectral luminosity of 1.1 $\times$ 10^{25} W Hz^{-1}. GRGs can play an important role in understanding the inter galactic medium (IGM) and structure formation.

GRGs are less common population of radio galaxies. After an active phase, which lasts for $\sim$10^7 $-$ 10^8 years, the AGN activity stops or falls to very low level such that the outflowing jets are no longer sustained. As a result, the radio core, jets and hot-spots on radio lobes disappears (Murgia et al., 2011). However, the radio lobes can be seen for some time before they disappear due to radiative losses. Thus, relic radio galaxy resulting from the cessation of AGN activity represents a short-lived final phase of radio galaxy evolution. The short-lived phase makes them a rare class of objects.

1.2 X-ray Imaging & Spectroscopy

X-ray astronomy is relatively new field as most of the X-rays are absorbed in the atmosphere and we needed satellites to observe X-ray radiation from space. Many astronomical objects emit, reflect or fluoresce X-rays. The objects include galaxy clusters, central regions of AGN, stars, X-ray binaries and supernova remnants.
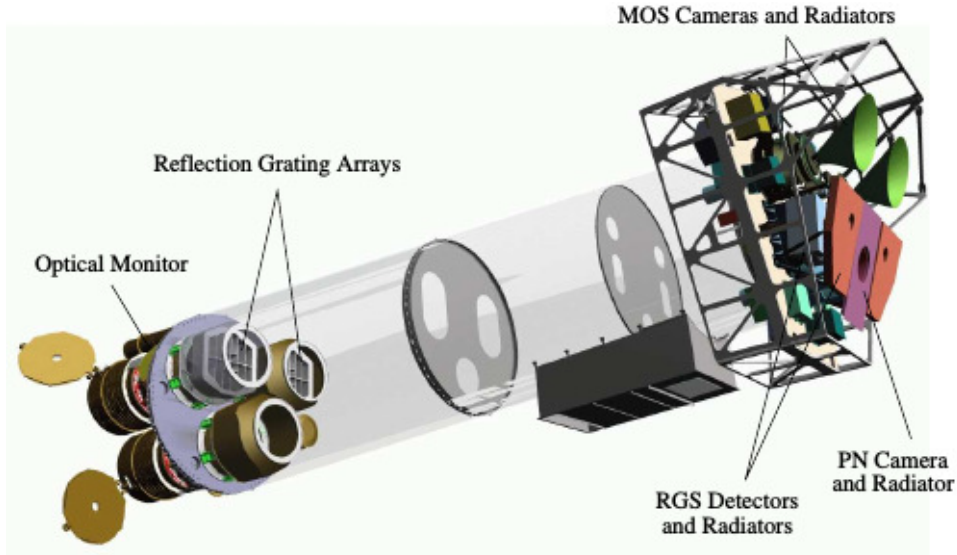
Figure 1.1: *Sketch of the XMM-Newton spacecraft with its payload. On the left-hand side, three telescopes can be seen. On the right-hand side, focal plane instruments can be seen, which include: two EPIC MOS cameras at the focus of two telescopes along with two Reflection Grating Arrays and an EPIC PN detector. The light from third telescope is focused on it, unattenuated. Image courtesy of Dornier Satellitensysteme GmbH.*

Several processes such as bremsstrahlung, black body radiation, synchrotron radiation and the inverse-Compton radiation gives rise to X-ray continuum, which constitutes a part of observed X-ray background.

As X-rays are very high energy photons, they behave more like particles rather than waves. So, it is possible to measure energy of each individual photon. Based on the type of detectors used in the X-ray telescopes, time of arrival of each photon can be recorded. Thus, X-rays produce a wide range of data in many forms.

The first observations in the X-ray band were made from instruments on rockets and balloons. The rockets reached an altitude greater than 100 km, and X-rays in the range ∼0.25–10 keV could be observed from them using Geiger counters. Rockets and balloons together detected X-rays from sources such as the Sun, the Crab nebula, the moon and diffuse X-ray background. As the technology progressed, X-ray satellites were launched in the space to observe the X-ray sky. Some of these satellites include ROSAT (Europe), EINSTEIN (USA) and ASCA (Japan). Currently, there are two major X-ray satellites orbiting the earth taking

data and producing exciting science, *CHANDRA* X-ray mission launched by NASA and *XMM-Newton* launched by European Space Agency. For our study, we used archival data from *XMM-Newton* telescope. Following subsection describes the properties of *XMM-Newton*.

1.2.1   XMM-Newton Telescope

The European Space Agency's X-ray Multi-Mirror satellite *XMM-Newton* was launched in December 1999. It carries two distinct types of telescope: three X-ray telescopes containing high precision concentric mirrors that focus incoming X-rays to a large field of view ($\sim 30'$) on three European Photon Imaging Cameras (EPIC), a 30 cm optical/UV telescope with a CCD detector at its focal plane and two Reflection Grating Spectrometers (RGS) for high-resolution X-ray spectroscopy (see Fig 1.1). *XMM-Newton* provides an angular resolution of $\sim 6'$ Full Width at Half Maximum (FWHM). Its high effective mirror area (~ 4300 cm^{-2} at 1.5 keV) is superior to all other X-ray observatories. Furthermore, it's highly eccentric orbit (travelling up to nearly one-third of the distance to the moon) allows very long and uninterrupted observations.

There are two types of EPIC CCD cameras for X-ray imaging, moderate resolution spectroscopy and X-ray photometry; two Metal Oxide Semiconductor (EPIC MOS) cameras and one EPIC PN camera. Each of the two EPIC MOS cameras consists of 7 chips, each with a matrix of 600×600 pixels. EPIC PN cameras are specifically developed for *XMM-Newton*. EPIC PN is illuminated from the back side, which doesn't have insensitive layers or coatings, as opposed to EPIC MOS, making it more sensitive to soft X-ray photons. Moreover, PN detectors have faster pixel readout time as compared to MOS detectors (0.03 ms of PN versus 1.5 ms of MOS in standard Timing Mode). All three EPIC detectors can take X-ray spectroscopic observations in the energy range of 0.2 − 12 keV.

1.3   Radio Interferometry

This section we review basics of radio interferometry adapted from Kadler (2005). Working of a radio interferometer is same as that of the Michelson interferometer.
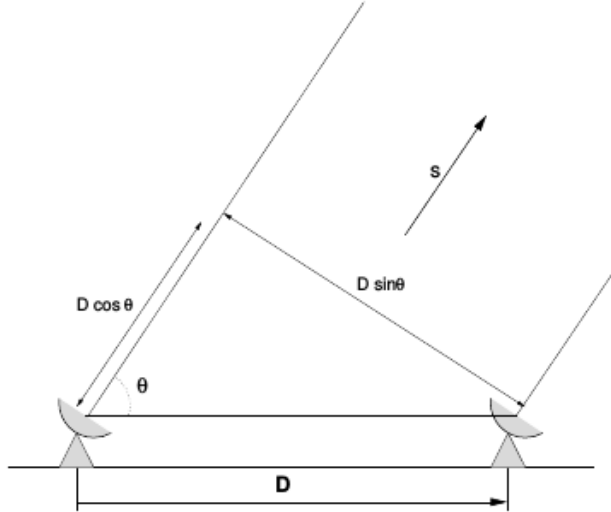
Figure 1.2: *An elementary radio interferometer. Image taken from Kadler (2005).*

Incoming rays from a distant source can be assumed to be parallel to each other (far-field pattern). When the rays fall on the antennas, voltages are created at the telescope backend, where they are correlated, i.e., a circuitry performs a multiplication and averaging of the voltages. If the source is a monochromatic emitter, then voltages are sinusoidal functions. Figure 1.2 shows that the signal reaches the first antenna at a time $\tau_g = (D/c)\cos\theta$ before it arrives at the second one, where D is the baseline of the two telescopes and c is the velocity of light. This is called the geometrical delay and the correlator output is proportional to

$$F = \sin(2\pi\nu t)\sin(2\pi\nu\,(t - \tau_g)). \tag{1.1}$$

The projected baseline $D\sin\theta$ varies with time as the earth rotates and so does the geometrical delay. The correlator output after filtering out the terms independent of τ_g, after some trigonometrical transformations is given by

$$F = \cos(2\pi\nu\tau_g\cos\theta). \tag{1.2}$$

Therefore, the correlator output is proportional to a quasi-sinusoidal fringe pattern, due to the rotation of the Earth. If the source has extended structure, the interferometer receives the signal not only from the direction s, where it is pointed at, but from a whole area around a nominal position s_0. Then, an element of solid angle $d\Omega$ of the source, from the position $s = s_0 + \sigma$, contributes

12

the power $1/2\Delta\nu\,B(\sigma)A(\sigma)d\Omega$ at each of the two antennas. $\Delta\nu$ is the observing bandwidth, $B(\sigma)$ is the brightness at position σ, $A(\sigma)$ is the reception pattern of the antenna, and the factor $1/2$ arises because of the capability of a telescope to receive only one direction of circular polarization. Correlating the two antenna output powers and applying the fringe term of above equation, the interferometer output becomes

$$r(D_\lambda, S_0) = \Delta\nu \int_{4\pi} A(\sigma)B(\sigma)\cos(2\pi\mathrm{D}_\lambda \cdot \mathrm{s})\,\mathrm{d}\Omega \qquad (1.3)$$

with $\nu\tau_g = D_\lambda \cdot s$, where D_λ is the vector of the baseline in units of the observing wavelength. Introducing a complex quantity

$$V = |V|e^{i\phi_V} \int_{4\pi} A_N(\sigma)B(\sigma)e^{-2\pi D_\lambda \cdot \sigma}\,d\Omega \qquad (1.4)$$

with a normalized reception pattern $A_N(\sigma) = A(\sigma)/A_0$, where A_0 is the antenna collecting area in direction s_0, the correlator output is

$$r(D_\lambda, S_0) = A_0\Delta\nu|V|\cos(2\pi\mathrm{D}_\lambda \cdot \mathrm{s}_0 - \phi_V). \qquad (1.5)$$

V is called the complex visibility. The correlator output can be expressed in terms of a fringe pattern with the modulus and phase of V. The phase is measured relative to the phase of a hypothetical fringe pattern received from a point source at the position s_0. Both, modulus and phase of V are observables, and Equation 1.4 shows that the visibility is the Fourier transform of the brightness distribution $B(\sigma)$. In order to reconstruct B, the visibility V has to be measured with different baselines D_λ. Usually this is expressed in terms of a two-dimensional plane with coordinates $u = D_\lambda^{E/W}\cos\theta$ and $v = D_\lambda^{N/S}\cos\theta$, which are basically the projected baselines in east–west and in north–south direction and are called spatial frequencies. This (u, v)–plane has to be sampled frequently enough in order to be able to perform a discrete Fourier transform of the measured visibility function $V(u, v)$ and thus retrieve the brightness distribution B of the source with an angular resolution determined by the highest spatial frequency of the interferometer.

Chapter 2

Theory

Most of the radio emission we see from radio galaxies is due to synchrotron radiation. It can also give rise to X-ray radiation. In the following sections, radiative processes producing radio and X-ray radiation related to our source are discussed.

2.1 Synchrotron Radiation

Synchrotron radiation is emitted when a charged particle moving at relativistic speeds moves in the presence of the magnetic field with component perpendicular to its velocity. When a non-relativistic charged particle moves in electric and magnetic field, it experiences Lorentz force given by:

$$F = q(E + \beta \times B) \tag{2.1}$$

where, β is velocity in units of speed of light. In the absence of electric field, the particles perform helical motion around the magnetic field with gyration frequency of its orbit also called as Larmor frequency given by,

$$\nu_B = qB_\perp/2\pi\gamma mc \tag{2.2}$$

where $\gamma = 1/\sqrt{1 - \beta^2}$ is Lorentz factor of the particle and $B_\perp$ is component of the magnetic field perpendicular to its velocity. It can be shown that the power radiated by the particle is given by

$$P = \frac{4}{3}\sigma_T c\gamma\beta^2 U_B \propto \gamma^2 U_B \tag{2.3}$$

where σ_T is Thomson cross section and $U_B = B^2/8\pi$ is energy density of the magnetic field.

In the case of a particle moving at relativistic speeds, relativistic doppler effect shifts the gyration frequency to

$$\nu'_B = \nu_B/(1 - \beta_\parallel \cos\theta) \tag{2.4}$$

where $\beta_\parallel$ is the parallel component of the velocity to the magnetic field and θ is the angle between v and B.

If we consider an ensemble of electrons with continuous energy distribution given by $n(E) = n_0 E^{-p}$, produce power law synchrotron spectrum where flux density

$$S_\nu \propto \nu^{-\alpha} \tag{2.5}$$

with the spectral index related to energy index p as

$$\alpha = \frac{p-1}{2}. \tag{2.6}$$

The energy density of the distribution of electrons given above is

$$U_e = \int_{E_1}^{E_2} n(E) E dE \tag{2.7}$$

Integrating above equation over source volume V gives a total energy in electrons

$$E_e = N_0(E_2^{2-p} - E_1^{2-p})/(2-p) \quad \text{(if p} \neq 2) \tag{2.8}$$

where $N_0 = n_0 V$ and $E_e = U_e V$. It can be shown that total power radiated by an electron is given as

$$-\frac{dE}{dt} = CB^2 E^2. \tag{2.9}$$

From eq 2.9 and eq 2.8, we can obtain luminosity of the source

$$L = \int_{E_1}^{E_2} CB^2 E^2 N_0 E^{-p} dE. \tag{2.10}$$

Integrating above equation for all energies and solving for N_0 gives total energy in the electrons (given here in terms of frequency and spectral index) as,

$$E_e = \frac{LC_1}{CB^{3/2}} \frac{2-2\alpha}{1-2\alpha} \frac{\nu_2^{1/2-\alpha} - \nu_1^{1/2-\alpha}}{\nu_2^{1-\alpha} - \nu_1^{1-\alpha}} \quad \left(\text{if } \alpha \neq \frac{1}{2} \text{ or } 1\right) \tag{2.11}$$

The energy is stored in the electrons as well as the magnetic field. Hence, total energy of the source is,

$$E_T = E_p + E_B = aAB^{-3/2} + VB^2/8\pi \qquad (2.12)$$

where E_p is energy in the particles, a is the ratio of energy in the protons to the energy in the electrons and V is the volume of the source. Here we have assumed that the magnetic field and particles fill the source volume uniformly. The above equation has minimum near the value of B for which E_p and E_B are equal. Thus, the minimum energy condition is

$$E_{min} = 0.5(aAL)^{4/7}V^{3/7} \qquad (2.13)$$

and corresponding minimum/equipartition magnetic field is given by

$$B_{E_{min}} \sim B_{eq} = (6\pi aAL/V)^{2/7} = 2.3(aAL/V)^{2/7}. \qquad (2.14)$$

For all the detailed calculations in this section, we refer the reader to Moffet (1975).

2.2   Inverse-Compton Radiation

Low energy photons can be up-scattered to very high energies by relativistic electrons. This process is called inverse-Compton scattering as it is opposite of Compton scattering. In the rest frame of the charge, a wave of frequency ν_i appears Doppler shifted to a frequency,

$$\nu_i' = \gamma\nu_i(1 - \beta\cos\theta) \qquad (2.15)$$

where θ is the angle of incidence in observer's frame of reference. In this frame, for non-relativistic electrons satisfying the condition $h\nu_i \gg m_e c^2/\gamma$, the scattered wave frequency is equal to the incident wave frequency ($\nu_f' = \nu_i'$). Moving back to the observer's frame of reference, the up-scattered frequency is given by,

$$\nu_f = \gamma^2\nu_i\left(1 - \beta\cos\theta\right)\left(1 + \beta\cos(\theta' + \psi')\right) \qquad (2.16)$$

where θ' and ψ' are angle of incidence and scattering, respectively, in the rest frame of the charge. For highly relativistic electrons ($\gamma \gg 1$), we often generally get,

$$\nu_f \sim \gamma^2\nu_i. \qquad (2.17)$$

16

Thus, for sufficiently high γ, photons can be up-scattered to very high frequencies.

It can be shown that for ultra-relativistic electrons ($\gamma \gg 1$) and for an isotropic radiation field of energy density U_{ph}, the power of scattered radiation is given by,

$$P = 2.6 \times 10^{-14} U_{ph} \gamma^2 \quad \text{erg/sec} \qquad (2.18)$$

This equation is very similar to eq 2.9 for synchrotron losses, the major difference being magnetic field energy density is replaced by photon field energy density. Hence, inverse-Compton losses become more important when $U_{ph} > B^2/8\pi$.

The above results were derived when Thomson cross-section can be used, i.e., when $h\nu'_i \sim \gamma h\nu_i \ll m_e c^2$. In the other extreme, when $\gamma h\nu_i \gg m_e c^2$, the Klein-Nishina formula applies and energy of scattered photons increase only logarithmically.

In this extreme case, using Klein-Nishina formula, it can be shown that for initial power law distribution of electrons with continuous energy distribution given by $n(E) = n_0 E^{-p}$, inverse-Compton scattering produces spectrum with spectral index $(p - 1)/2$ (for detailed calculations, see Tucker (1977)). Hence, for a given electron distribution producing synchrotron and inverse-Compton radiation, shapes of synchrotron and inverse-Compton spectrum are identical.

The seed photon field can be provided by various sources. The most common photon field is the Cosmic Microwave Background (CMB) that is universally present everywhere. In the hotspots of the radio lobes, the seed photon field can be synchrotron photons produced by relativistic particles. They can be up-scattered by particles themselves who produced them. This special case of inverse-Compton scattering is called Self Synchrotron Compton (SSC).

2.3   Thermal Plasma Emission

Thermal emission means that the energy of the plasma can be characterized by the temperature of the electrons. Nature and processes of thermal emission depend on the plasma temperature. For temperatures less than 5×10^6 K (~ 0.43 keV) line emission from various ionized atoms in the gas dominates. For temperatures greater than that, thermal bremsstrahlung continuum emission dominates (also

called as free-free emission).

Exact shape of the spectrum depends on a variety of parameters, pressure, density, metallicity, temperature. In general, emission line forest if superimposed on thermal bremsstrahlung continuum. Relative strengths of lines and maximum temperature of the plasma depends on temperature of the plasma. The scaling of the thermal plasma emission is proportional to the product of electron and hydrogen density integrated over the volume of the emitting plasma, the so called emission measure (EM) $= \int n_e n_H dV$.

Chapter 3

Observations and data analysis techniques

The high redshift GRG discussed was discovered in the XMM-LSS field. The GRG lies in a smaller subfield of the XMM-LSS field, known as the SXDF field at RA $2^h16^m59^s$ and DEC $-4^d49^m20.6^s$ (J2000). This subfield has some of the deepest available observations, particularly in the near-infrared, mid-infrared and radio bands. In this work, we have combined our GMRT continuum observations at 0.325 GHz with archival X-ray imaging from XMM-Newton, and 1.4 GHz VLA images from Simpson et al. (2006). We used Optical imaging and spectroscopy from Subaru, ultra deep JHK band near-infrared imaging from the UKIDSS-UDS survey, deep Spitzer imaging in the 4 IRAC bands and the 24 micron MIPS band from the SpUDS survey for host galaxy identification and photometric redshift calculation.

3.1   Radio Observations

The 0.325 GHz image was obtained by Wadadekar et al. 2015 (in prep.) using the Giant Metrewave Radio Telescope (GMRT) observation of the XMM-LSS field covering over $\sim$ 12 sq degrees with a 16-pointing mosaic. Scans were carried out in semi-snapshot mode of 6-17 minutes each to optimize the uv-coverage. This resulted in uniform sensitivity in the central region, where this source lies. The final map has an average 1σ rms noise of $\sim$ 150 μJy beam^{-1}. The 0.325 GHz

19

Table 3.1: *Radio flux densities of the giant radio galaxy.*

	$S_{1.4\ GHz}$	$S_{0.610\ GHz}$	$S_{0.610\ GHz}$	$S_{0.325\ GHz}$	$S_{0.240\ GHz}$	$\alpha^{1.4}_{0.325}$
	int	int	int	int	int	
	(mJy)	(mJy)	(mJy)	(mJy)	(mJy)	
North Lobe	5.8±0.10	13.6±2.4	-	79.8±5.20	49.5±7.4	1.79±0.11
South Lobe	3.8±0.90	6.6±1.4	-	60.2±4.52	53.6±7.0	1.89±0.12
Total	9.6±0.14	20.2±2.7	43.3	140±6.9	169.1±20.2	1.83±0.08

Note. Column 1: flux density at 1.4 GHz measured using 1.4 GHz radio image. Column 2 is 0.610 GHz flux density taken from Tasse et al. (2007). Column 3 is taken from Vardoulaki et al. (2008). Column 4 is 0.325 GHz radio flux density calculated using the 0.325 GHz GMRT image. Column 5 is flux density at 0.240 GHz taken from Tasse et al. (2007). Column 6 is the spectral index calculated using 0.325 GHz and 1.4 GHz fluxes. All flux densities are integrated flux densities of individual component or of the entire source.

GMRT image has a synthesized beam of $9.35'' \times 7.38''$ at a position angle (PA) $=73.25°$.

The 1.4 GHz radio image was obtained by Simpson et al. (2006) using the VLA in its B and C array configuration. The 1.4 GHz image rms noise is $\sim 20-22$ μJy[1]. The 1.4 GHz VLA image has a synthesized beam of $\sim 5'' \times 4''$ at PA $\sim 70°$.

Tasse et al. (2007) have observed the XMM-LSS field at 0.240 GHz and 0.610 GHz using GMRT. 0.240 and 0.610 GHz GMRT observations cover 18.0 and 12.7 deg^2 with noise-rms ~ 2.5 and ~ 0.3 mJy beam^{-1} and resolutions of $14''.7$ and $6''.5$ arcsec, respectively. There are deeper 0.610 GHz GMRT observations of the SXDF field covering 0.5 deg^{-2} with noise-rms of ~ 60 μJy beam^{-1}, with a synthesized beam of $6''.8 \times 5''.4$ at position angle (PA) of 30° (see Vardoulaki et al., 2008). The total 0.610 GHz flux density of the GRG estimated from deeper GMRT observations in the SXDF field is 43.3 mJy. This clearly shows that a significant flux is missed in shallow observations reported in Tasse et al. (2007). Therefore, we use 0.610 GHz flux density given in Vardoulaki et al. (2008) in our analysis. The total flux density of the GRG is 140 mJy at 0.325 GHz and 9.6 mJy at 1.4 GHz. Table 3.1 summarizes radio flux densities of the lobes.

3.1.1 Missing flux density issue

This part was done by Dr. Aritra Basu, MPIfR, Germany. The total flux density from large angular extent source can be underestimated due to under sampling of the $uv-$plane at the lowest $uv-$distance. This could be significant at higher radio frequencies. An interferometer with the shortest baseline $D_{\min}$ can detect all the flux from angular scales less than $\sim 0.6\lambda/D_{\min}$, provided the uv-plane is densely sampled at the shortest spacings. Here, λ is the observing wavelength. The total angular extent of the GRG is ~ 2 arcmin at 0.325 GHz, and can be well sampled by baselines having uv-length $\gtrsim 1$ kiloλ. This is not an issue with the GMRT observations at 0.325 GHz, as the shortest baseline starts from ~ 150 λ. Hence, we do not believe that there is any missing flux density at 0.325 GHz and all the structures are well recovered. However, the 1.4 GHz observations using B- and C-array configuration of the VLA, the uv-plane is sampled from 1 kiloλ to 17kλ.

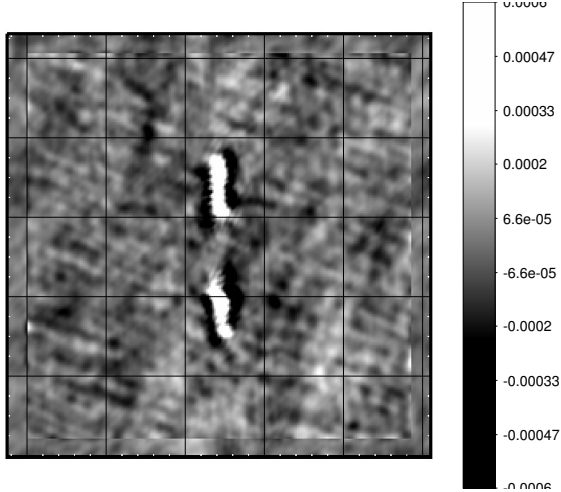[1]1 Jy $= 10^{-26}$ W m^{-2} Hz$^{-1} = 10^{-26}$ erg s^{-1} cm^{-2} Hz^{-1}

Figure 3.1: *Residual image after subtracting the GMRT map at 0.325 GHz with the model map imaged using the uv−coverage at 1.4 GHz. The residual image is in units of Jy beam^{-1}.*

This is just enough to recover all angular scales of the GRG.

The amount of missing flux at 1.4 GHz using the VLA observations was tested in the following way. We sampled the 0.325 GHz map observed using the GMRT with the $uv-$coverage of the 1.4 GHz observations using the VLA in B- and C-array configuration. This allowed to produce model $uv-$data for the full extent of the GRG. This model data was subsequently imaged using the same deconvolution parameters as used by Simpson et al. (2006). The model image has total flux density of 152 mJy as compared to the original flux density of 156 mJy within the 3σ contour. This allows us to quantify the extent of missing flux density at 1.4 GHz to be $\lesssim 3$ percent. In Figure 3.1 we show the residual image after subtracting the 0.325 GHz GMRT image with the re-sampled model image. The residual image has rms noise of ~ 150 μJy beam^{-1}, similar to that of the rms noise of the 0.325 GHz GMRT image. This also indicates that all the structures could be well recovered at 1.4 GHz. Additionally, we compared the 1.4 GHz radio flux with NRAO VLA Sky Survey observations, they are comparable indicating that there is very little or no radio flux missing as a result of radio interferometric undersampling. Hence, we do not expect missing flux density in 1.4 GHz map.
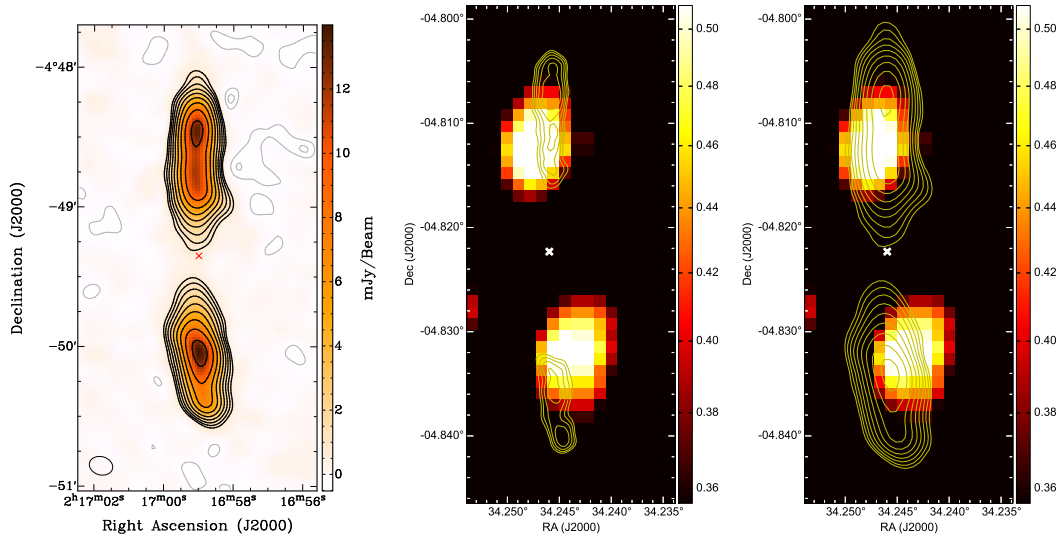
Figure 3.2: *Left panel : Grey scale 0.325 GHz GMRT image of our relic GRG J021659-044920. Middle Panel : 0.325 GHz contours overlaid on the soft band (0.3 - 2.0 keV) EPIC pn image. Right panel : 1.4 GHz contours overlaid on the soft band (0.3 - 2.0 keV) EPIC pn image. Lowest radio contour is at 5σ level with successive contours increased by $\sqrt{2}$. The X-ray image is smoothed with a Gaussian of kernel radius $5''.0$. Marker x indicates the position of the host galaxy.*

3.2 X-ray Observation

We used XMM-Newton archival data with observation ID 0112372001 (PI: Dr. Michael Watson). The data were taken in prime-full window mode using thin filter on 7th January, 2003 and consist of 25.63 ks EPIC PN and 27.35 ks of EPIC MOS data. We discuss the extraction of X-ray spectrum in section 3.5. Figure 3.2 shows the smoothed X-ray image with GMRT and VLA radio contours overlaid. The diffuse X-ray emission is nearly co-spatial with 0.325 GHz GMRT radio contours, but, it is offset from 1.4 GHz VLA contours.

3.3 Optical/Near Infrared Identification

The core of the host galaxy is not detected in radio (0.325 GHz, 1.4 GHz images) or in X-ray. To find the host galaxy we use optical identification given in Vardoulaki et al. (2008). Optical data is obtained in five photometric bands (B, V, r, i', z') from Subaru telescope (Simpson et al., 2006). To understand the nature of
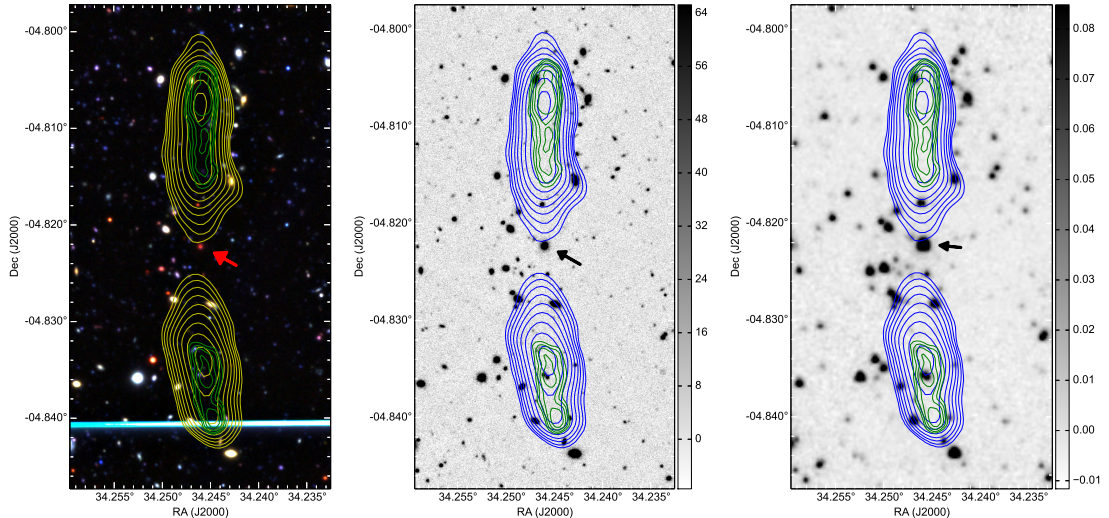
Figure 3.3: *Left panel: 0.325 GHz (in yellow) and 1.4 GHz (in green) radio contours overlaid on the three-color optical RGB image. RGB 3-color image obtained by combining Subaru B band (blue), R band (green) and z′ band (red) images. An artefact due to a foreground bright star is seen as a bluish white horizontal bar at the lower end of the image. Extreme red colour of the host galaxy is apparent in RGB image. Central and Right panel: UKIDSS K band and SpUDS 4.5 μm images, respectively. In all images, lowest radio contour is at 5σ level with successive contours increased by $\sqrt{2}$. Green contours are 1.4 GHz and blue contours are 0.325 GHz radio contours. In each panel, the arrow points to the host galaxy.*

host galaxy, we also use near-IR (J, H and K bands) and mid-IR data (3.6, 4.2, 5.8 and 8 micron) from UK Infrared Deep Sky Survey's (UKIDDS) Ultra Deep Survey (UDS) and Spitzer UKIDSS Ultra Deep Survey (SpUDS), respectively. The host galaxy is a very red galaxy (B−K = 7), almost exactly at the center of the radio contours. There are no other sources in the vicinity of this source, which can be considered as plausible host galaxy candidates. We consider it a reliable identification. Figure 3.3 shows UKIDSS UDS K-band image with GMRT 0.325 GHz radio contours and 1.4 GHz VLA contours.

The optical and IR band magnitudes of this galaxy are listed in Table 3.2. Subaru optical band magnitudes (B to z') are taken from Simpson et al. (2006), near infrared band magnitudes (J, H, K) are taken from UKIDSS UDS DR8 catalog and mid-infrared fluxes are measured using aperture photometry from the SpUDS images. The host galaxy is not detected in 24 μm MIPS band. MIPS has 5σ limit

Table 3.2: *AB magnitudes of the host galaxy in the optical and infrared bands.*

Band	B	V	R	i'	z'	J	H	K
Magnitude	25.08	24.62	23.96	22.98	22.02	20.30	19.23	18.13

Band	3.6μm	4.5μm	5.8μm	8μm
Magnitude	17.83	17.91	18.66	19.23

Note. Optical band magnitudes (BVRi'z') are from the Subaru, near infrared fluxes (JHK) are from the UKIDSS-UDS catalog and mid-infrared fluxes (3.6,4.5,5.6,8μm) were measured by us from the SpUDS images using fixed aperture of $6''$ diameter.

of 40μJy.

3.4   Photometric redshift estimation

The spectroscopic redshift provided by Vardoulaki et al. (2008) is based on a low S/N spectrum of an extremely red galaxy. Deep panchromatic observations from UKIRT and Spitzer, allows us to independently estimate the photometric redshift of the host galaxy. We calculated photometric redshift of the source by fitting template SEDs to the photometric data available for the host AGN using the publicly available photometric redshift estimation code EAZY[2] by, (Brammer et al., 2008). The EAZY code combines a number of features from various existing codes. It is able to fit a linear combination of templates and its templates are based on semi-analytical models, rather than observed spectra of galaxies.

For photometry we used fixed aperture of $6''$ diameter to calculate the flux density of the source in the four IRAC bands of SpUDS. Note that this was done since, unlike in the other bands, a SpUDS catalog is not currently available. For the purpose of galaxy template fitting, we used optical (Subaru), near infrared (UKIDSS-UDS) and mid-infrared (SpUDS) data. The fitting gave photometric redshift $z_{phot} = 1.26^{+0.24}_{-0.15}$. The spectroscopic redshift $z_{spec} = 1.325$ lies within 1σ limit of z_{phot}. Figure 3.4 shows the best fit template.

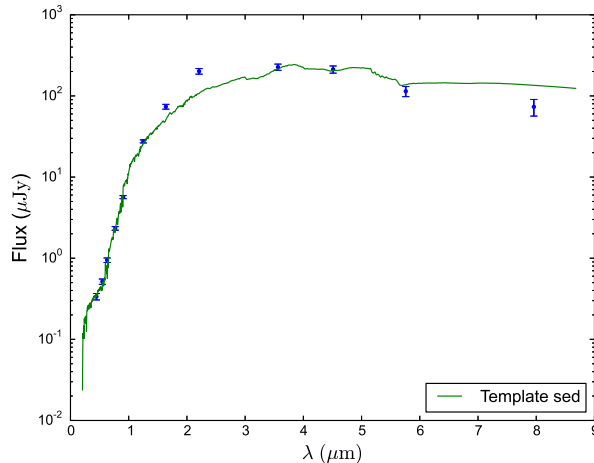
[2]http://www.astro.yale.edu/eazy/

Figure 3.4: *Best fit galaxy template (green curve) for the observed photometric data points (blue). The best fit template SED is a linear combination of default SED templates, and a dusty galaxy template provided on the EAZY website.*

3.5   X-ray data analysis

We used XMM-Newton's Science Analysis System (SAS) version 13.5 for data reduction. Observations Data Files (ODF) were processed with `emproc` and `epproc` commands to produce calibrated and concatenated event lists for EPIC cameras. These files were filtered for flaring particle background using standard recommended PATTERN, FLAG, and energy filters to generate clean files for spectrum extraction, and to produce images. The number of counts were insufficient to fit the spectrum for each lobe separately. Hence, spectrum of total extended emission containing both lobes was extracted in 0.3–10 keV energy range and fitted using XSPEC v12.8.2. Spectrum was extracted from elliptical regions for both the lobes as shown in Figure 3.2 and source free local background regions were selected for background spectrum. We used galactic absorption column value $N_H = 2.52 \times 10^{20} \mathrm{cm}^{-2}$, using the 'Colden: Galactic Neutral Hydrogen Density Calculator' tool provided by NASA's CHANDRA X-ray Observatory, operated by the Smithsonian Astrophysical Observatory. MOS1 and MOS2 spectra had insufficient number of counts to constrain the spectrum well, hence we used PN spectrum of the entire source. PN spectrum was binned in minimum 20 background-subtracted counts per bin.

First, we fitted the spectrum with power-law model modified by galactic ab-
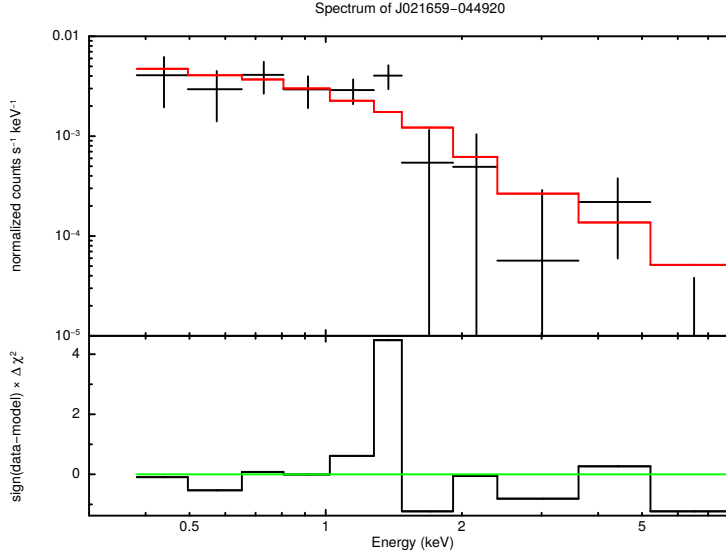
Figure 3.5: *0.3 – 10 keV XMM-N pn spectrum best fitted with an absorbed power law, where absorbing column density is fixed to the galactic value. Solid red line and crosses ('+') represent fitted model and binned data points, respectively. Residuals are shown in the bottom panel.*

sorption. Then to investigate thermal origin of the observed X-rays, we fitted the spectrum with MEKAL model modified by galactic absorption. The MEKAL model represents an emission spectrum from hot diffuse gas based on the model calculations of Mewe et al. (1986). For both models, galactic absorption column value was fixed to the value mentioned above. For MEKAL model, relative abundance was fixed to 0.6, based on the best fit value from a range of relative abundance from 0.1 to 1.5. The parameters of these fits are presented in Table 3.3.

Table 3.3: *Best-fit parameters for the power-law and* MEKAL *spectral models for total extended X-ray emission from the lobes. Errors represent 90 per cent confidence interval for all parameters.*

Model	Parameter	Value
Power law	K_{norm}	$5.29^{+1.30}_{-1.30} \times 10^{-6}$
	N_H (cm^{-2}) (fixed)	2.52×10^{20}
	Γ	$1.86^{+0.49}_{-0.41}$
	$\chi^2/$dof	$9.7/11$
	$0.3 - 10$ keV flux (erg cm^{-2} s^{-1})	3.25×10^{-14}
	$2.0 - 10$ keV flux (erg cm^{-2} s^{-1})	1.69×10^{-14}
MEKAL		
	K_{norm}	$7.90^{+1.09}_{-1.93} \times 10^{-5}$
	kT (keV)	$4.2^{+15.3}_{-2.3}$
	nH (cm^{-3})	1.17×10^{-2}
	Abundance	0.6
	$\chi^2/$dof	$9.27/10$

Chapter 4

Results

A spectroscopic redshift of $z = 1.325$ was reported for this source by Vardoulaki et al. (2008), based on FOCAS/Subaru spectrum (Furusawa et al., 2008). At $z = 1.325$, one arcminute represents 513 kpc in the plane of the sky for our chosen cosmological parameters. It spans $2'.4$ on the sky which represents a projected size of 1.2 Mpc. Features like a jet, hotspot and core are absent in the radio images. Because, the hotspots are not visible, we used end to end size of 5σ contour at 0.325 GHz to measure the size of the GRG.

4.1   Radio and X-ray spectral index

Under ICCMB, it is expected that the non-thermal X-ray spectrum will have similar spectral shape to the radio spectrum. This implies that the spectral index in the radio should be the same as the slope of the X-ray spectrum. In our observations, we find that the radio spectral index, α is in the range 1.5 and 2.5 (see Figure 4.1). The X-ray emission photon index, Γ, is related to the X-ray spectral index (α_{Xray}) as, $\alpha_{\text{Xray}} = \Gamma - 1$. We obtain, $\Gamma = 1.86^{+0.49}_{-0.41}$, which corresponds to $\alpha_{\text{Xray}} = 0.86^{+0.49}_{-0.41}$. The slope in X-rays is therefore significantly different from that in the radio.

In terms of energy, electrons emitting between 0.76 and 3.25 GHz in the restframe (i.e., 0.325 and 1.4 GHz in the observed-frame), correspond to the energy range ~ 3.6 and 7.6 GeV for magnetic field strengths of 3.5 μG. Thus, the Lorentz factor (γ_e) of the electrons are $\sim 7 \times 10^3$ and $\sim 1.5 \times 10^4$, respectively. For CMB

photons at $z = 1.325$, having temperature 6.34 K, the Planck function peaks at $\nu_{bg} \approx 6.6 \times 10^{11}$ Hz. These photons are up-scattered by the CR electrons in the radio to X-ray frequencies with average frequencies given by $\langle \nu \rangle \approx (4/3)\gamma^2 \nu_{bg}$. Thus, the CR electrons emitting at rest frame 0.76 and 3.25 GHz would up-scatter these CMB photons to 4.3×10^{19} and 2×10^{20} Hz, i.e., energies in the range $\sim$175 and 830 keV. Thus, our X-ray observations between $\sim$ 0.5 and 5 keV, corresponding to 1.16 and 11.6 keV in the rest frame do not probe this steep part of the spectrum. In our observed range of X-ray energies, the emission arises due to IC scattering with CR electrons at much lower radio frequencies where the spectral index is expected to be flatter than that between 0.76 and 3.25 GHz. In this way, the different spectral indices as measured in the X-ray and radio data may be reconciled.

4.2 Spectral index map

We computed spectral index maps of the lobes of the GRG using 0.325 GHz GMRT and 1.4 GHz VLA data (see Figure 4.1). 0.325 GHz radio emission extends well beyond 1.4 GHz radio emission in the lobes. Spectral index map shows steepening of the spectral index towards the inner parts of the lobes nearer to the host galaxy. Spectral index steepens from 1.4 near the outer edge of the lobes away from the host galaxy to 2.5 near the host galaxy. The average spectral index of the north lobe is 1.78, and of the south lobe is 1.9 (see Table 3.1). The spectral index is extremely steep relative to typical low z radio galaxies where it is $\sim$ 0.7 (Blundell et al., 1999)). This variation of the spectral index with the distance from the nucleus in the lobes is consistent with the backflow model of the lobes (Leahy and Williams, 1984; Leahy et al., 1989). According to this model, pressure in the hotspot re-accelerates the post-shock material back towards the core, creating a backflow. The older part of the backflow material (part towards the core) loses energy making the spectrum steep in this part of the lobes.

Using X-ray emission alone, we can estimate the lower limit on the total energy in the relativistic electrons. We follow equation (4) of Erlund et al. (2006):
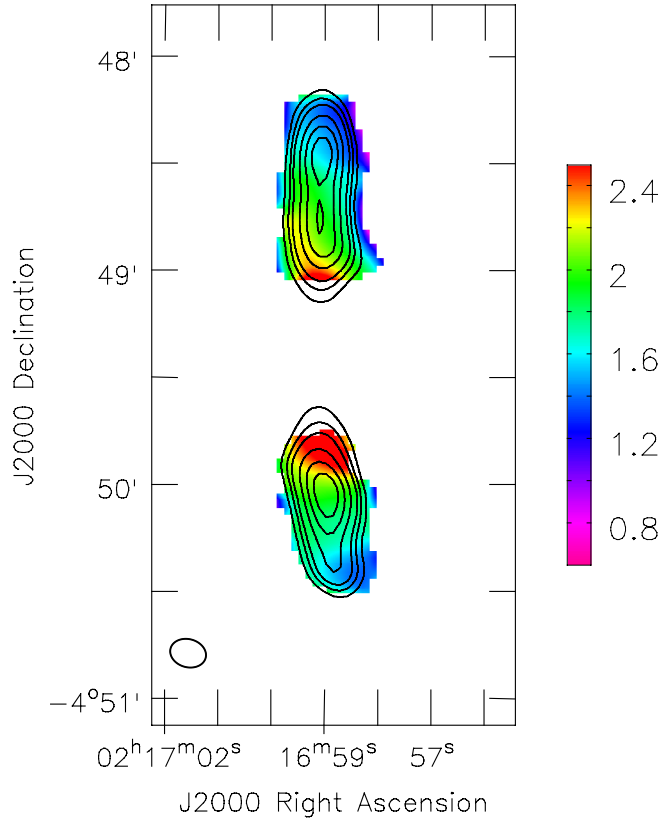
Figure 4.1: *Spectral index map of the lobes of the giant radio galaxy obtained from 0.325 GHz GMRT and 1.4 GHz VLA data with 0.325 GHz GMRT contours.*

$$\varepsilon_e = \frac{3}{4} \frac{L_{44}}{\gamma_e (1+z)^4} 10^{64} \text{ erg,} \tag{4.1}$$

where L_{44} is the X-ray luminosity in 10^{44} erg s^{-1} and γ_e is the typical Lorentz factor of the electrons responsible for ICCMB. Assuming $\gamma_e = 10^3$ gives $\varepsilon_e = 4.2 \times 10^{59}$ erg.

Chapter 5

Discussion

The core and hotspots of the GRG are not detected either in the X-ray or the radio. This indicates that the host AGN is either not active, or it is heavily absorbed with a flat or an inverted radio spectrum. We note that the 1.4 GHz VLA observation (rms $\sim$20–22 μJy) is significantly deeper than the 0.325 GHz radio observation. If the core had a flat or inverted radio spectrum, it should have been detected in the 1.4 GHz observation. Thus, the absence of jets, hotspots and a core together with an extremely steep radio spectrum is a strong indicator that the central activity has stopped since the extended source was produced.

We have detected diffuse X-ray emission associated with the lobes of J021659-044920. Spectral fitting is not able to differentiate between power-law and MEKAL models. The X-ray spectrum is best fitted with power-law of photon index Γ = $1.86^{+0.49}_{-0.41}$ modified by galactic absorption, and thermal MEKAL model giving thermal temperature of $4.2^{+15.3}_{-2.3}$ keV. Thermal temperature of the plasma is high and poorly constrained. Density of thermal electrons required for the model is $n_{th} \sim 1.17 \times 10^{-2}$ cm^{-3}. We follow argument of Isobe et al. (2005), that this value is too high compared to the values of $n_{th} \ll 10^{-3}$ cm^{-3} indicated by a number of studies on radio polarimetry effects. Also, since jet activity has stopped, the plasma is unlikely to be shock-heated to produce thermal X-ray emission. Therefore, we conclude that the observed X-ray emission is of non-thermal origin and thermal plasma in the lobes has negligible contribution to it.

The X-ray spectral index is flatter than radio spectral index. X-ray emission is nearly co-spatial with the radio lobes. When the jets are active, the electrons are

shock accelerated in the hotspots with initial power-law distribution of spectral index ~ 0.5 (Croston et al., 2005). Then cooling processes such as adiabatic expansion of the lobes, synchrotron radiation and ICCMB steepened the spectral index to observable frequencies. We discuss these processes and arguments for ICCMB in the following subsections.

5.1   Energy losses

The electrons in the hotspots are further accelerated to relativistic energies through diffusive shock acceleration. Under such a scenario, the cosmic ray electrons are injected with spectral index given by, $\alpha_{\mathrm{inj}} = (M^2 + 3)/(2M^2 - 2)$ (Blandford and Eichler, 1987), where M is the Mach number. For strong shocks, i.e., $M \gg 1$, the electrons are injected with a typical spectral index of 0.5. These relativistic electrons undergo energy losses that modify the injected power law spectrum. The dominant energy loss processes are synchrotron, inverse-Compton cooling and adiabatic cooling. Synchrotron and IC losses have the effect of steepening the spectrum and leads to a cutoff at higher radio frequencies ($\gtrsim 1$ GHz), while adiabatic losses do not affect the spectrum. We, therefore, ignore adiabatic losses from our discussion.

Both, synchrotron and IC losses affect the spectrum in a similar way, wherein, the spectrum is smoothly steepened at higher frequencies. The spectrum is characterised by a break frequency, ν_{br}, below which the spectrum remains a power law with a spectral index identical to the injection spectral index (α_{inj}). Above ν_{br}, the form of the steepening depends on the mechanism of particle injection. For steady continuous injection of relativistic electrons (CI model), the spectrum steepens by 0.5 (Pacholczyk, 1970). For single shot particle injection, the spectrum falls off as a power law with index $4\alpha_{\mathrm{inj}}/3 + 1$ above the break frequency, assuming constant pitch angle between electrons and magnetic field (KP model; Kardashev, 1962; Pacholczyk, 1970). However, considering rapid isotropization of the pitch angle distribution leads to an exponential cut-off above the break frequency (JP model; Jaffe and Perola, 1973).

In Figure 5.1 (left-hand panel) we show the expected spectral index between
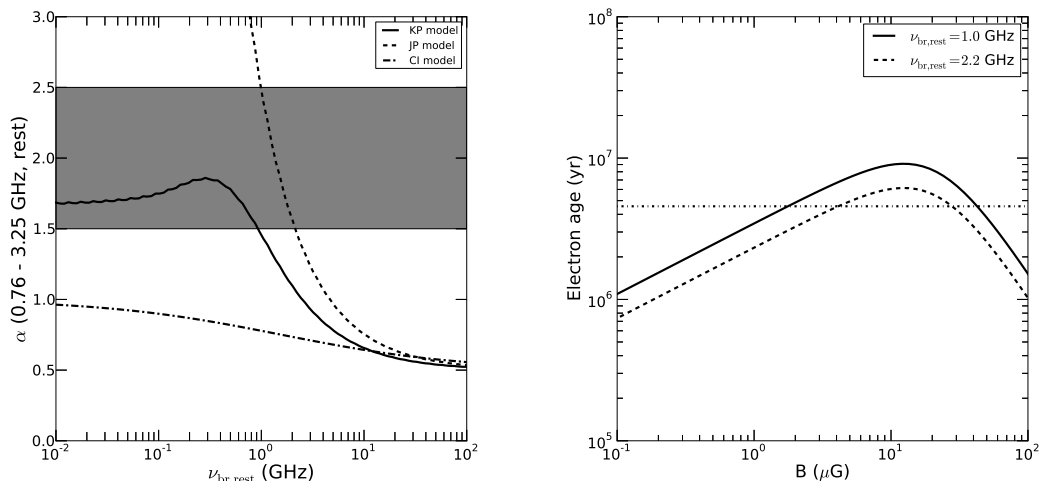
Figure 5.1: *Left-hand panel: The expected spectral index between rest-frame 0.76 and 3.25 GHz as a function of the break frequency at rest-frame, $\nu_{\mathrm{br,rest}}$ for the various models of particle injection with $\alpha_{\mathrm{inj}} = 0.5$. The shaded region shows the observed range of the spectral index in the lobes. Right-hand panel: Expected age of the electrons as a function of the magnetic field strength (B) for $\nu_{\mathrm{br,rest}}$ at 1.0 and 2.2 GHz. The dashed-dot line shows the time required for the electrons to fill up the lobes assuming a jet velocity of 0.3c. (The images were obtained by Dr. Aritra Basu.)*

rest-frame 0.76 and 3.25 GHz for the different models described above for $\alpha_{\mathrm{inj}} = 0.5$. The shaded region shows the observed range of the spectral index in the lobes. Clearly, the CI model cannot explain the observed steepness. For CI model to explain our observations, $\alpha_{\mathrm{inj}} > 1$ is required, which is generally not the case. The fact that the extended radio emission is very bright at low radio frequencies and extends well beyond high-frequency radio emission together with the observed spectral index supports the fact that the lobes consist of an old population of electrons that were injected into the IGM from a now discontinued jet activity.

5.2   Arguments for ICCMB in the lobes

From Figure 5.1 (left-hand panel), it is clear that CI and KP models cannot give rise to the observed steepening of the spectral index. As per the JP model, the range of the spectral index suggests, $\nu_{\mathrm{br,rest}}$ to be in the range 1 to 2.2 GHz in the rest-frame. For the JP model, ν_{br} depends on the age of the electrons (t) and the

magnetic field strength (B) as,

$$\frac{\nu_{\text{br}}}{\text{GHz}} = 1.12 \times 10^{15} \left(\frac{B}{\text{G}}\right) \left[\left\{\frac{2}{3}\left(\frac{B}{\text{G}}\right)^2 + \left(\frac{B_{\text{IC}}}{\text{G}}\right)^2\right\}\left(\frac{t}{\text{s}}\right)\right]^{-2} \quad (5.1)$$

Here, B_{IC} is the equivalent magnetic field strength for IC scattering. In our case, the IC scattering is with the CMB and $B_{\text{IC}} \approx 3.25(1 + z)^2$ μG. Putting $z = 1.325$ in the above equation gives, $B_{\text{IC}} \approx 17.5$ μG.

In Figure 5.1 (right-hand panel) we plot the age of the electrons as a function of the magnetic field strength (B) using Equation (1). The dashed-dot line shows the time required for the electrons to fill up the lobes of size ~ 420 kpc at the distance of the GRG. We assumed a typical bulk velocity of the electrons as $0.3c$. Now, for the observed steepening to be caused by synchrotron losses alone, $B \gg B_{\text{IC}} \sim 17.5$ μG is required. It is clear from the figure that, if $B \gtrsim 30$ μG, then synchrotron timescales would be less than the time required to fill the observed size of the lobe. This allows us to put an upper limit on the magnetic field strength as < 30 μG. The upper limit of the field strength is comparable to the equivalent IC field strength. Hence, it is unlikely that synchrotron losses alone could give rise to the observed steepening of the spectral index. Furthermore, clear detection of the lobes at 1.4 GHz allows us to put a lower limit on the magnetic field strength of ~ 3 μG. Otherwise, IC losses would completely dominate at 1.4 GHz and would not allow any detectable synchrotron emission.

Assuming ICCMB, we can estimate the magnetic field in the lobes from X-ray flux. We use the formula given in Tucker (1977) to estimate the magnetic field in the lobes:

$$\begin{aligned}\frac{F_c}{F_s} &= 2.47 \times 10^{-19} \left(5.23 \times 10^3\right)^\alpha \left(\frac{T}{1K}\right)^{3+\alpha} \\ &\times \frac{b(n)}{a(n)} \left(\frac{B}{1G}\right)^{-(\alpha+1)} \left(\frac{\nu_c}{\nu_s}\right)^{-\alpha}\end{aligned} \quad (5.2)$$

where B is the magnetic field strength in the lobes of the giant radio galaxy, T is the temperature of the CMB at the redshift of the source, ν_c is frequency of inverse-Compton X-ray emission, ν_s is frequency of radio synchrotron emission and the constants $a(n)$ and $b(n)$ are taken from Ginzburg and Syrovatskii (1965)

and Tucker (1977), respectively.

This analysis requires the observed X-ray and radio fluxes to be cospatial. To get the cospatial flux, we extracted the source spectrum in a region matching the 5σ contours of the 0.325 GHz image, and fitted the spectrum with absorbed power law model with N_H set to galactic absorption. The best fit gave a photon index $\Gamma = 1.77^{+0.51}_{-0.42}$ corresponding to spectral index of $0.77^{+0.51}_{-0.42}$. The rest frame unabsorbed 2–10 keV cospatial flux $F_c = 1.44 \times 10^{-14}$ erg s^{-1} cm^{-2} (0.75 nJy for bandwidth of $\sim$8 keV). Taking the flux density of the synchrotron emission $F_s = 140$ mJy at 0.325 GHz, $\alpha = 0.77$ and $h\nu_c \approx 3$ keV yields a magnetic field of 3.3 μG. Taking $\alpha = 0.86$ gives $B = 3.6$ μG. These values of the magnetic field are consistent with the upper (30 μG) and lower limit (3 μG) on the magnetic fields as discussed above, further supporting the ICCMB interpretation.

We can also independently calculate the magnetic field using equipartition argument (see Moffet (1975), equation 2.77). We use the 0.325 GHz lobe size. We assume radio-emitting lobes of our GRG to be cylindrical in shape. We take each lobe to be ~ 500 kpc long and ~ 180 kpc in diameter, $\nu_{min} = 10$ MHz and $\nu_{max} = 10$ GHz. Note that 1.4 GHz flux density is heavily affected by ICCMB losses. This analysis is valid only for synchrotron losses. Therefore, the observed spectral index of 1.83 is not valid in this case. As discussed earlier, synchrotron losses steepen the spectrum by 0.5. For $\alpha_{inj} = 0.5$ synchrotron losses would steepen the spectral index to $\alpha = 1.0$. Using $\alpha = 1.0$ and the other values mentioned above gives an equipartition magnetic field $B_{eq} = 3.5$ μG. This value also lies within the limits on the magnetic field.

Chapter 6

Conclusion

In this thesis, we study the a GRG J021659-044920 at high redshift ($z \sim 1.3$), ~ 8.97 Gyr into the past. The GRG display X-ray emission caused by inverse Compton scattering of cosmic microwave background photons. Using the radio and X-ray observations we are able to:

- conclude that the host AGN activity has stopped recently

- conclude that the observed difference in X-ray and radio spectral indices is because we are observing X-rays upscattered by population of low energy electrons in the lobes, they are least affected by spectral ageing

- conclude that observed steepening of the radio spectral index is due to the backflow mechanism

- estimate the minimum energy in the lobes to be $\varepsilon_e = 4.2 \times 10^{59}$ erg

- use the ratio of X-ray to radio fluxes to compute the magnetic field to be 3.3 μG

- estimate the equipartition magnetic field to be $B_{eq} = 3.5$ μG.

The GRG we discovered, is one of less than a dozen of ICCMB X-ray emitting FR-II galaxies at high redshift discovered till date. Their study provides us with a direct measurement of the properties of the magnetic field and the energetics in these galaxies in the distant universe.

References

C. Scharf, I. Smail, R. Ivison, R. Bower, W. van Breugel, and M. Reuland, "Extended X-Ray Emission around 4C 41.17 at z = 3.8", *ApJ* **596** (2003) 105–113, `astro-ph/0306314`.

O. Johnson, O. Almaini, P. N. Best, and J. Dunlop, "0.5 Mpc-scale extended X-ray emission in the z = 2.48 radio galaxy 4C 23.56", *MNRAS* **376** (2007) 151–156, `astro-ph/0608656`.

A. C. Fabian, S. Chapman, C. M. Casey, F. Bauer, and K. M. Blundell, "The extended X-ray emission around HDF130 at z = 1.99: an inverse Compton ghost of a giant radio source in the Chandra Deep Field-North", *MNRAS* **395** (2009) L67–L70, `arXiv:0902.3117`.

K. M. Blundell, A. C. Fabian, C. S. Crawford, M. C. Erlund, and A. Celotti, "Discovery of the Low-Energy Cutoff in a Powerful Giant Radio Galaxy", *ApJ* **644** (2006) L13–L16, `astro-ph/0605391`.

M. C. Erlund, A. C. Fabian, and K. M. Blundell, "The inverse Compton X-ray-emitting lobes of the high-redshift giant radio galaxy 6C0905+39", *MNRAS* **386** (2008) 1774–1780, `0803.1545`.

A. C. Fabian, J. S. Sanders, C. S. Crawford, and S. Ettori, "A deep Chandra observation of the cluster environment of the z= 1.786 radio galaxy 3C 294", *MNRAS* **341** (2003) 729–738, `astro-ph/0301468`.

D. A. Schwartz, "X-Ray Jets as Cosmic Beacons", *ApJ* **569** (2002) L23–L26.

B. L. Fanaroff and J. M. Riley, "The morphology of extragalactic radio sources of high and low luminosity", *MNRAS* **167** (1974) 31P–36P.

M. C. Erlund, A. C. Fabian, K. M. Blundell, A. Celotti, and C. S. Crawford,
"Extended inverse-Compton emission from distant, powerful radio galaxies",
MNRAS **371** (2006) 29–37, `astro-ph/0606238`.

J.-C. Mauduit, M. Lacy, D. Farrah, J. A. Surace, M. Jarvis, S. Oliver,
C. Maraston, M. Vaccari, L. Marchetti, G. Zeimann, E. A. Gonzáles-Solares,
J. Pforr, A. O. Petric, B. Henriques, P. A. Thomas, J. Afonso, A. Rettura,
G. Wilson, J. T. Falder, J. E. Geach, M. Huynh, R. P. Norris, N. Seymour,
G. T. Richards, S. A. Stanford, D. M. Alexander, R. H. Becker, P. N. Best,
L. Bizzocchi, D. Bonfield, N. Castro, A. Cava, S. Chapman, N. Christopher,
D. L. Clements, G. Covone, N. Dubois, J. S. Dunlop, E. Dyke, A. Edge, H. C.
Ferguson, S. Foucaud, A. Franceschini, R. R. Gal, J. K. Grant, M. Grossi,
E. Hatziminaoglou, S. Hickey, J. A. Hodge, J.-S. Huang, R. J. Ivison, M. Kim,
O. LeFevre, M. Lehnert, C. J. Lonsdale, L. M. Lubin, R. J. McLure,
H. Messias, A. Martínez-Sansigre, A. M. J. Mortier, D. M. Nielsen, M. Ouchi,
G. Parish, I. Perez-Fournon, M. Pierre, S. Rawlings, A. Readhead, S. E.
Ridgway, D. Rigopoulou, A. K. Romer, I. G. Rosebloom, H. J. A. Rottgering,
M. Rowan-Robinson, A. Sajina, C. J. Simpson, I. Smail, G. K. Squires, J. A.
Stevens, R. Taylor, M. Trichas, T. Urrutia, E. van Kampen, A. Verma, and
C. K. Xu, "The Spitzer Extragalactic Representative Volume Survey (SERVS):
Survey Definition and Goals", *PASP* **124** (2012) 714–736, `arXiv:1206.4060`.

A. K. Kembhavi and J. V. Narlikar, "Quasars and active galactic nuclei : an
introduction", 1999.

M. Murgia, P. Parma, K.-H. Mack, H. R. de Ruiter, R. Fanti, F. Govoni,
A. Tarchi, S. Giacintucci, and M. Markevitch, "Dying radio galaxies in
clusters", *A&A* **526** (2011) A148, `arXiv:1011.0567`.

M. Kadler, "Compact Radio Cores in AGN: The X-ray Connection", PhD thesis,
University of Bonn, Germany, 2005.

A. T. Moffet, *Strong Nonthermal Radio Emission from Galaxies*, p. 211. the
University of Chicago Press, 1975.

W. H. Tucker, "Radiation processes in astrophysics.", 1977.

C. Simpson, A. Martínez-Sansigre, S. Rawlings, R. Ivison, M. Akiyama, K. Sekiguchi, T. Takata, Y. Ueda, and M. Watson, "Radio imaging of the Subaru/XMM-Newton Deep Field - I. The 100-μJy catalogue, optical identifications, and the nature of the faint radio source population", *MNRAS* **372** (2006) 741–757, `astro-ph/0609529`.

C. Tasse, H. J. A. Röttgering, P. N. Best, A. S. Cohen, M. Pierre, and R. Wilman, "GMRT observations of the XMM large scale structure survey field", *A&A* **471** (2007) 1105–1116.

E. Vardoulaki, S. Rawlings, C. Simpson, D. G. Bonfield, R. J. Ivison, and E. Ibar, "Radio imaging of the Subaru/XMM-Newton Deep Field - II. The 37 brightest radio sources", *MNRAS* **387** (2008) 505–535, `0803.2801`.

G. B. Brammer, P. G. van Dokkum, and P. Coppi, "EAZY: A Fast, Public Photometric Redshift Code", *ApJ* **686** (2008) 1503–1513, `0807.1533`.

R. Mewe, J. R. Lemen, and G. H. J. van den Oord, "Calculated X-radiation from optically thin plasmas. VI - Improved calculations for continuum emission and approximation formulae for nonrelativistic average Gaunt factors", *A&AS* **65** (1986) 511–536.

H. Furusawa, G. Kosugi, M. Akiyama, T. Takata, K. Sekiguchi, I. Tanaka, I. Iwata, M. Kajisawa, N. Yasuda, M. Doi, M. Ouchi, C. Simpson, K. Shimasaku, T. Yamada, J. Furusawa, T. Morokuma, C. M. Ishida, K. Aoki, T. Fuse, M. Imanishi, M. Iye, H. Karoji, N. Kobayashi, T. Kodama, Y. Komiyama, Y. Maeda, S. Miyazaki, Y. Mizumoto, F. Nakata, J. Noumaru, R. Ogasawara, S. Okamura, T. Saito, T. Sasaki, Y. Ueda, and M. Yoshida, "The Subaru/XMM-Newton Deep Survey (SXDS). II. Optical Imaging and Photometric Catalogs", *ApJS* **176** (2008) 1–18, `0801.4017`.

K. M. Blundell, S. Rawlings, and C. J. Willott, "The Nature and Evolution of Classical Double Radio Sources from Complete Samples", *AJ* **117** (1999) 677–706, `astro-ph/9810197`.

J. P. Leahy and A. G. Williams, "The bridges of classical double radio sources", *MNRAS* **210** (1984) 929–951.

J. P. Leahy, T. W. B. Muxlow, and P. W. Stephens, "151-MHz and 1.5-GHz observations of bridges in powerful extragalactic radio sources", *MNRAS* **239** (1989) 401–440.

N. Isobe, K. Makishima, M. Tashiro, and S. Hong, "The XMM-Newton Detection of Diffuse Inverse Compton X-Rays from Lobes of the FR II Radio Galaxy 3C 98", *ApJ* **632** (2005) 781–787, `astro-ph/0506682`.

J. H. Croston, M. J. Hardcastle, D. E. Harris, E. Belsole, M. Birkinshaw, and D. M. Worrall, "An X-Ray Study of Magnetic Field Strengths and Particle Content in the Lobes of FR II Radio Sources", *ApJ* **626** (2005) 733–747, `astro-ph/0503203`.

R. Blandford and D. Eichler, "Particle acceleration at astrophysical shocks: A theory of cosmic ray origin", *Phys. Rep.* **154** (1987) 1–75.

A. G. Pacholczyk, "Radio astrophysics. Nonthermal processes in galactic and extragalactic sources", 1970.

N. S. Kardashev, "Nonstationarity of Spectra of Young Sources of Nonthermal Radio Emission", *SvA* **6** (1962) 317.

W. J. Jaffe and G. C. Perola, "Dynamical Models of Tailed Radio Sources in Clusters of Galaxies", *A&A* **26** (1973) 423.

V. L. Ginzburg and S. I. Syrovatskii, "Cosmic Magnetobremsstrahlung (synchrotron Radiation)", **3** (1965) 297.